

## Neutral-particle production in 100-GeV/c $\bar{p}p$ interactions

R. Raja, C. Moore, L. Voyvodic, and R. J. Walker  
*Fermi National Accelerator Laboratory, Batavia, Illinois 60510\**

R. E. Ansorge, C. P. Bust, J. R. Carter, W. W. Neale, J. G. Rushbrooke, and D. R. Ward  
*Cavendish Laboratory, Cambridge, England†*

B. Y. Oh, M. Pratap, G. Sionakides, G. A. Smith, and J. Whitmore  
*Department of Physics, Michigan State University,‡ East Lansing, Michigan 48824*  
 (Received 1 October 1976)

We have investigated the inclusive production of  $\gamma$ ,  $K_S^0$ ,  $\Lambda^0$ , and  $\bar{\Lambda}^0$  in 100-GeV/c  $\bar{p}p$  interactions in the 30-in. hydrogen bubble chamber at Fermilab. We present various inclusive distributions and compare them with corresponding distributions in 100-GeV/c  $pp$  interactions and lower-energy  $\bar{p}p$  interactions. We find some evidence for  $\Sigma(1385)$  production but none for  $K^*(890)$  production. We find evidence for a nonzero  $\Lambda^0$  polarization of  $-0.45 \pm 0.21$ .

### I. INTRODUCTION

We present results on the inclusive production of  $\gamma$ ,  $K_S^0$ ,  $\Lambda^0$ , and  $\bar{\Lambda}^0$  in 100-GeV/c  $\bar{p}p$  interactions. The data described in this paper were obtained from a 98 000-picture exposure of the 30-in. bubble chamber at Fermilab incorporating the downstream wide-gap spark-chamber system. Charged-multiplicity distributions of  $\bar{p}p$  events and their differences with respect to corresponding  $pp$  data have already been published.<sup>1,2</sup> In this report we extend these comparisons between  $\bar{p}p$  and  $pp$  events to neutral-particle production and attempt where possible to ascertain the nature of this difference. A preliminary description of the data being presented in this paper has been published elsewhere.<sup>3</sup>

From a Regge analysis of the imaginary part of the forward elastic amplitude, it is possible to conclude<sup>4</sup> that

$$\sigma_{\bar{p}p}^{\text{tot}} - \sigma_{pp}^{\text{tot}} \propto s^{\alpha_\omega(0)-1}, \quad (1)$$

where  $\alpha_\omega(0) \simeq 0.4$  is the intercept of the  $\omega$  trajectory. It can also be argued that the difference between the  $\bar{p}p$  and  $pp$  total cross sections is mainly due to the annihilation channels present in  $\bar{p}p$ . On the basis of a generalized multi-Regge model developed by Chew, Goldberger, and Low,<sup>5</sup> it is possible to show<sup>6</sup> that annihilation channels produced by baryon exchange can sum up via unitarity to generate the difference (1). Recently, however, Eylon and Harari<sup>7</sup> have argued on the basis of a dual model that the annihilation channels sum up via unitarity to contribute to the Pomeron term in  $\sigma_{\text{tot}}(\bar{p}p)$ , and that the nonannihilation channels contribute to the  $\omega$  and  $\rho$  exchanges in the elastic amplitude. This then implies that the difference in cross sections (1), which falls with  $s$  to the power

$\alpha_\omega(0) - 1$ , is due in part to nonannihilation processes. Nonetheless, one can still hope to gain some insight into annihilation processes by studying differences, and in fact previous data from this experiment showed<sup>2</sup> that such a nonannihilation contribution might be small.

Experimental details are described in Secs. II and III, and in Sec. IV we consider topological cross sections neutral production and investigate their scaling properties with regard to lower-energy data. We also consider the implications of the multiperipheral model of Goldberg<sup>8</sup> for  $\pi^0$  production in annihilations. Section V describes longitudinal-momentum distributions, with particular regard to scaling, and Sec. VI examines transverse-momentum distributions. We subsequently discuss effective masses, missing masses, polarization effects, and multiple production of neutrals.

### II. EXPERIMENTAL DETAILS

*a. The beam.* The beam of 100-GeV/c antiprotons was obtained from the decay of  $\bar{\Lambda}^0$  particles produced by the interactions of 300-GeV/c protons in a copper target. The charged secondaries from the target were swept away and the  $\bar{\Lambda}^0$  particles were allowed to decay in a vacuum pipe. The beam line downstream of the primary target was tuned to accept 100-GeV/c negatives. This resulted in a  $\bar{p}/\pi^-$  ratio of  $\sim 1:4$  in the bubble chamber.<sup>9</sup> By triggering the bubble-chamber flash whenever two or more  $\bar{p}$ 's entered the chamber or whenever a  $\bar{p}$  interacted, it was possible to obtain a  $\bar{p}/\pi^-$  interaction ratio of 1:1.

*b. Fiducial-volume cuts and fitting procedure.* We have scanned for and measured all events with an associated "vee." For secondary vertices we

employed a fiducial volume whose dimensions were determined by the constraint that it be the largest volume visible in all three views. No event whose primary vertex was more than 10 cm downstream from the center of the chamber was accepted. The measured events were processed by the computer programs TVGP and SQUAW for geometric reconstruction and kinematic fitting. Where possible, ambiguities were resolved at the scanning table by comparing predicted and observed ionizations. The remaining ambiguities were eliminated by examining the fitted transverse-momentum ( $p_T$ ) distribution of the tracks of the vee relative to the neutral-particle direction. The maximum  $p_T$  for an electron pair is  $\sim 20$  MeV/ $c$ , so any ambiguities with  $p_T < 20$  MeV/ $c$  were assigned to the  $\gamma$  hypothesis. The maximum value of  $p_T$  for a  $K_S^0$  decay is 206 MeV/ $c$ , whereas for a  $\Lambda^0$  ( $\bar{\Lambda}^0$ ) it is 100 MeV/ $c$ . By distributing the  $K_S^0/\Lambda^0$  ambiguities in a manner consistent with the requirement that both  $p_T$  distributions have the desired shape, the remaining  $K_S^0/\Lambda^0$  ambiguities were resolved statistically. We estimate that the impurities in any one channel are less than 5% after these corrections have been applied. Our detection efficiency for  $\bar{\Lambda}^0$  decays is poor since most  $\bar{\Lambda}^0$ 's go forward in the laboratory with large momenta. The same is true for forward-going  $\Lambda^0$ 's. We correct for the loss of fast  $\Lambda^0$ 's by reflecting the  $\bar{\Lambda}^0$  events that occur in the backward hemisphere in the center of mass,<sup>10</sup> a valid procedure owing to  $C$  invariance. Unless otherwise stated no  $\bar{\Lambda}^0$  information will be explicitly presented, since all  $\bar{\Lambda}^0$  distributions may be obtained from the  $\Lambda^0$  distributions by inversion in the center of mass.

### III. SCANNING EFFICIENCIES AND WEIGHTS

To each event in the fiducial volume the following weight was attached:

$$\text{weight} = \frac{1}{e^{-L_{\text{min}}/L_0} - e^{-L_{\text{pot}}/L_0}},$$

where  $L_{\text{pot}}$  is the potential length of the vee (i.e., the path length from the primary vertex to the edge of the fiducial volume),  $L_{\text{min}}$  is the minimum length permitted between the primary and the secondary vertices ( $= 2$  cm for  $K_S^0$  and 3 cm for  $\Lambda^0/\bar{\Lambda}^0$  and  $\gamma$ ) (the scanning losses for vees closer to the vertex than  $L_{\text{min}}$  were deemed to be too large to be accurately determined by a second scan), and

$$\begin{aligned} \frac{1}{L_0} &= \frac{1}{L_D} + \frac{1}{L_I} \text{ for } \Lambda^0 \text{ and } K_S^0 \\ &= \frac{1}{L_I} \text{ for } \gamma, \end{aligned}$$

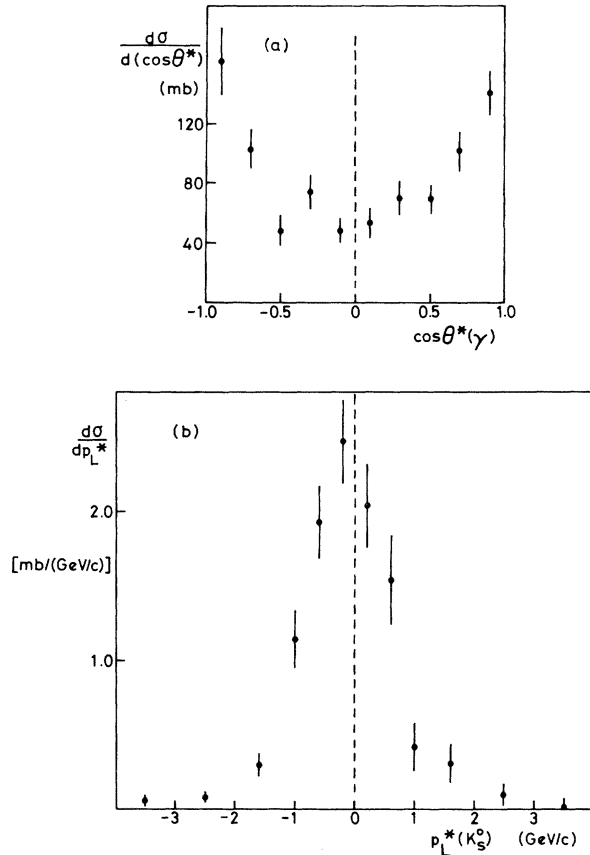


FIG. 1. (a) Distribution of c.m.-system angle,  $\cos\theta^*$ , for  $\gamma$ 's after weighting. Events with  $p_{\text{lab}} < 40$  MeV/ $c$  and corresponding forward  $\gamma$ 's are not included. (b) Longitudinal-momentum distribution in c.m. system for  $K_S^0$ . Note the depletion for  $p_L^* > 0$ .

where  $L_D$  is the decay length of the strange particle and  $L_I$  is the interaction length of the particle.

The correction due to interaction is small for  $\Lambda^0$  and  $K_S^0$  events, so their interaction lengths were computed by assuming constant total cross sections of 35 mb and 25 mb, respectively. These values are the total cross sections for  $\Lambda^0 p$  scattering<sup>11</sup> and the average of  $K^+ p$  and  $K^- p$  scattering<sup>12</sup> at the mean laboratory momenta of the  $\Lambda^0$  and  $K_S^0$ , respectively. For  $\gamma$ 's with laboratory momenta greater than 40 MeV/ $c$ , the cross section for pair production was parametrized as a function of momentum.<sup>13</sup> The pair-production cross section falls rapidly for momenta below 40 MeV/ $c$ , leading to large weights. It was therefore decided to reject  $\gamma$ 's with laboratory momenta less than 40 MeV/ $c$  and to correct for this loss by doubling the weights of those forward  $\gamma$ 's that yield laboratory momenta less than 40 MeV/ $c$  when inverted in the center of mass. This procedure is valid since, owing to  $C$  invariance, there is inversion symme-

try in the center of mass for  $\gamma$ 's. The  $\cos\theta^*$  distribution, with these slow  $\gamma$ 's and their corresponding partners removed, is symmetric about  $\cos\theta^*=0$  [Fig. 1(a)], which indicates that the scanning efficiency for the very forward  $\gamma$ 's is similar to that for  $\gamma$ 's going backward in the center of mass.<sup>14</sup>

The  $K_S^0$  longitudinal-momentum distribution in the center of mass ( $p_{\parallel}^*$ ) shows losses for positive  $p_{\parallel}^*$  [Fig. 1(b)]. It was therefore decided to ignore all forward-going  $K_S^0$  and to double the weights of those in the backward hemisphere, invoking  $C$  invariance once more. The weight for each event was corrected for the net scanning/measuring efficiency for that channel. For the strange particles, the weights were further corrected for unseen decay modes by dividing by the branching ratio<sup>15</sup> of the observed decay mode. Table I gives the scanning efficiencies and average weights for each channel.

#### IV. INCLUSIVE TOTAL AND TOPOLOGICAL CROSS SECTIONS COMPARISON WITH MULTIPERIPHERAL-MODEL PREDICTIONS

The weights thus obtained were normalized so that the total number of  $\bar{p}p$  interactions with charged multiplicity  $\geq 4$  in the primary-vertex fiducial volume corresponded to a cross section of  $31.0 \pm 0.5$  mb.<sup>1</sup> The cross sections are given in Ref. 3, which also makes a detailed comparison of  $\bar{p}p$  and  $pp$  inclusive cross sections.

Dao and Whitmore<sup>16</sup> have proposed an extension of Koba-Nielsen-Olesen (KNO) scaling for  $\pi^0$  production,

$$\frac{\langle n \rangle \sigma_n(\pi^0)}{\langle n_{\pi^0} \rangle \sigma_{\text{inel}}} = \Phi(n/\langle n \rangle), \quad (4)$$

and an analogous relationship has been applied by Cohen<sup>17</sup> to  $K_S^0$  and  $\Lambda^0$  production in  $pp$  interactions at high energies. In Figs. 2(a)–2(c) we plot  $\langle n \rangle \sigma_n(V^0)/\langle n_{V^0} \rangle \sigma_{\text{inel}}$  against  $n/\langle n \rangle$  for  $\pi^0$ ,  $K_S^0$ , and  $\Lambda^0$  production in  $\bar{p}p$  interactions from 4.6 to 100 GeV/c.<sup>18</sup> For comparison, the fits of Refs. 16 and 17 to high-energy  $pp$  interactions are also shown. We see that the  $\pi^0$  and  $K_S^0$  topological cross sections scale well over the whole energy range and lie on top of the  $pp$  curves. In contrast, the  $\Lambda^0$  data do not scale, the low-multiplicity points falling and the high-multiplicity points rising with increasing energy. The 100-GeV/c  $\bar{p}p \rightarrow \Lambda^0$  points agree quite well with  $pp$  data, suggesting that scaling may have been achieved by this energy.

Goldberg<sup>8</sup> has adapted the multi-Regge model of Chew, Goldberger, and Low to describe the annihilation process  $\bar{p}p \rightarrow (m)\pi^-(m)\pi^+(k)\pi^0$ . Using the "strong-ordering approximation," which assumes

TABLE I. Scanning efficiencies and weights.

	$\gamma$	$K_S^0$	$\Lambda^0$
Scanning efficiency	92.5%	92.4%	92.4%
Measuring efficiency	94.5%	94.5%	94.5%
Kinematics efficiency	95.4%	97.0%	97.0%
Mean decay weight	59.3	2.75	2.28
Standard deviation	38.0	1.46	0.91
Mean net weight	71.02	3.23	2.68
Standard deviation	45.56	1.72	1.08

that the different multiperipheral graphs do not interfere, he finds

$$\sigma_{m,k} = G^4 e^{(2\alpha_B - 2)Y} (g^2 Y)^{2m+k-2} \left(\frac{1}{3}\right)^k \left(\frac{2}{3}\right)^{2m} \times \frac{(2m+k)!}{k! 2m! (2m+k-2)!}, \quad (5)$$

where  $\sigma_{m,k}$  is the cross section for  $\bar{p}p$  annihilation into  $(m)\pi^-$ ,  $(m)\pi^+$ , and  $(k)\pi^0$ . The notation follows Ref. 8. From (5) the topological cross section  $\sigma_m$  for the process  $\bar{p}p \rightarrow (m)\pi^-(m)\pi^+$  may be computed, yielding

$$\sigma_m = \sum_{k=0}^{\infty} \sigma_{m,k} = G^4 e^{(2\alpha_B - 2 + g^2/3)Y} \times \left[ \frac{4}{9} \frac{(\frac{2}{3}g^2 Y)^{2m-2}}{(2m-2)!} + \frac{4}{9} \frac{(\frac{2}{3}g^2 Y)^{2m-1}}{(2m-1)!} + \frac{1}{9} \frac{(\frac{2}{3}g^2 Y)^{2m}}{(2m)!} \right]$$

and

$$\sigma_{\text{annih}} = \sum_{m=0}^{\infty} \sigma_m \approx \frac{1}{2} G^4 e^{(2\alpha_B - 2 + g^2)Y}. \quad (6)$$

Following Goldberg we now impose the bootstrap condition that

$$2\alpha_B - 2 + g^2 = \alpha_{\omega}(0) - 1 \approx -0.6, \quad (7)$$

assuming that  $\sigma_{\text{annih}} = \sigma_{\bar{p}p}(\text{tot}) - \sigma_{pp}(\text{tot})$ . If one now further assumes that  $\sigma_m$  is the difference in topological cross sections between  $\bar{p}p$  and  $pp$  (Ref. 19) multiplicity  $n=2m$ , one can fit the differences to Eq. (6) subject to the constraint (7). Table II contains a summary of the results of such a fit.<sup>20</sup>

We can now predict the difference between  $\bar{p}p \rightarrow \pi^0$  and  $pp \rightarrow \pi^0$  inclusive cross sections as a function of the charged multiplicity. However, the errors are large so that only the gross features may be trusted. Using Eq. (5) we derive

$$\begin{aligned} \sigma_n(\bar{p}p \rightarrow \pi^0) - \sigma_n(pp \rightarrow \pi^0) &= \sum_{k=0}^{\infty} k \sigma_{m,k} \quad (n=2m) \\ &= G^4 \frac{e^{(2\alpha_B - 2)Y}}{2m!} (g^2 Y)^{2m-2} \left(\frac{2}{3}\right)^{2m} e^x \\ &\quad \times [2m(2m+1)x + 2(2m+1)x^2 + x^3], \quad (8) \end{aligned}$$

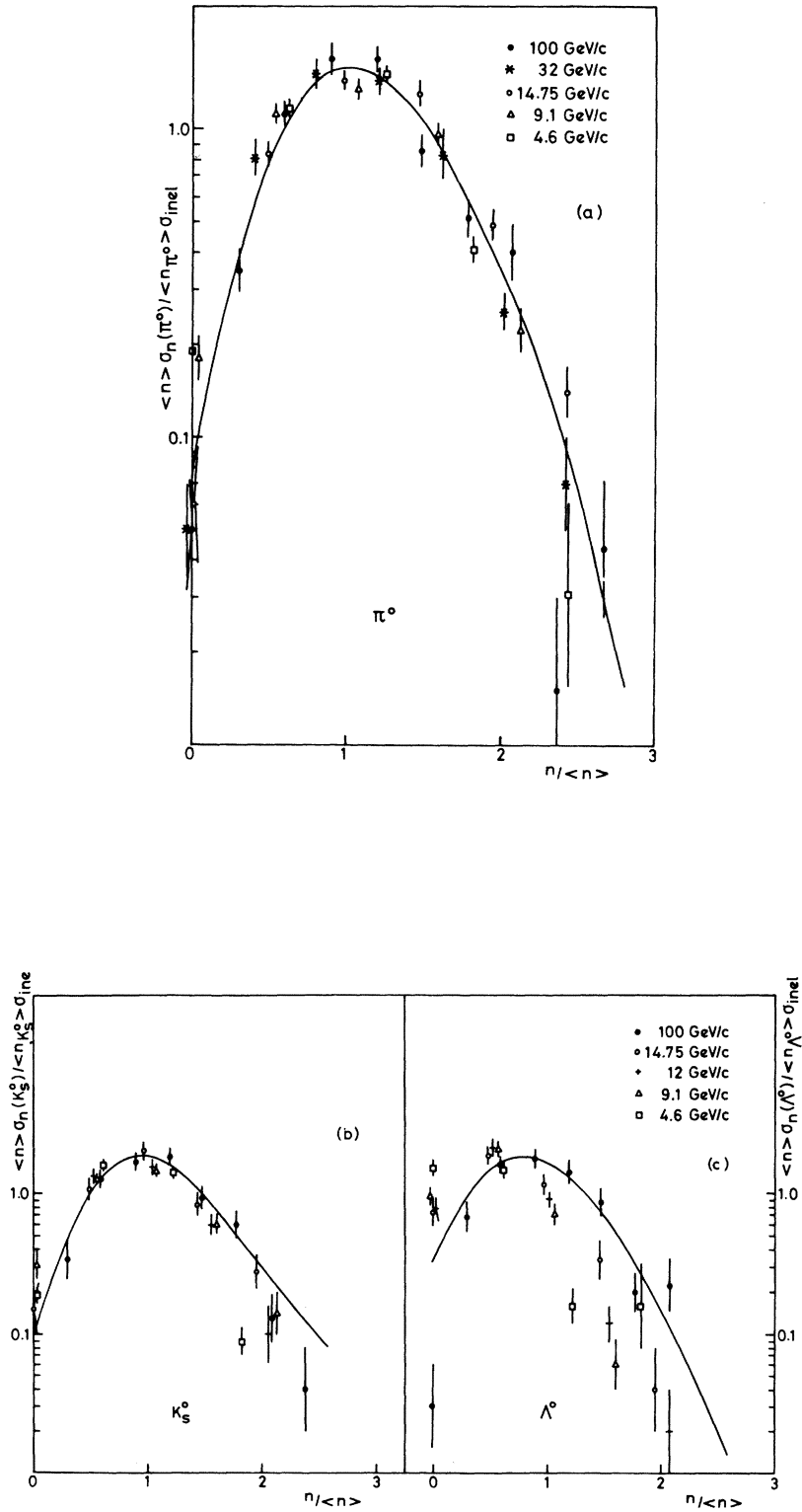


FIG. 2. Scaling of topological cross sections. (a)  $\langle n \rangle \sigma_n(\pi^0) / \langle n_{\pi^0} \rangle \sigma_{inel}$  against  $n / \langle n \rangle$  for  $\bar{p}p \rightarrow \pi^0$  at various energies. (b) for  $K_S^0$  (c) for  $\Lambda^0$ . The curves are fits to high-energy  $pp$  data.

TABLE II. Multiperipheral analysis.

Prong	Experimental values $\sigma_n(\bar{p}p) - \sigma_n(pp)$ (mb) smoothed	Fitted $\sigma_n(\bar{p}p) - \sigma_n(pp)$ (mb)	Experimental $\sigma_n(\bar{p}p \rightarrow \pi^0) - \sigma_n(pp \rightarrow \pi^0)$ (mb)	Predicted values $\sigma_n(\bar{p}p \rightarrow \pi^0) - \sigma_n(pp \rightarrow \pi^0)$ (mb)	Predicted $\langle \pi^0 \rangle$ for annihilations
4	$0.30 \pm 0.28$	$0.12 \pm 0.05$	$0.90 \pm 1.90$	$0.63 \pm 0.23$	$5.33 \pm 1.30$
6	$0.65 \pm 0.28$	$0.44 \pm 0.14$	$0.00 \pm 4.90$	$2.24 \pm 0.56$	$5.11 \pm 1.25$
8	$1.13 \pm 0.35$	$0.80 \pm 0.15$	$2.70 \pm 3.00$	$4.01 \pm 0.56$	$4.97 \pm 1.25$
10	$0.61 \pm 0.28$	$0.88 \pm 0.10$	$0.70 \pm 1.80$	$4.25 \pm 0.60$	$4.86 \pm 1.20$
12	$0.34 \pm 0.27$	$0.62 \pm 0.12$	$0.60 \pm 1.40$	$2.97 \pm 0.79$	$4.78 \pm 1.20$
14	$0.30 \pm 0.08$	$0.31 \pm 0.10$	$2.90 \pm 1.92$	$1.46 \pm 0.63$	$4.72 \pm 1.20$
16	$0.15 \pm 0.06$	$0.11 \pm 0.08$	$-0.80 \pm 0.45$	$0.53 \pm 0.50$	$4.67 \pm 1.10$
18	$0.07 \pm 0.03$	$0.03 \pm 0.07$	$0.10 \pm 0.64$	$0.15 \pm 0.40$	$4.63 \pm 1.10$
Total	$3.55 \pm 0.66$ mb	$3.32 \pm 0.38$ mb	$7.10 \pm 6.7$ mb	$16.3 \pm 2.0$ mb	

Fitted values:  $G^4 = 167 \pm 20$  mb  
 $g^2 = 2.36 \pm 0.6$   
 $\alpha_B = -0.48 \pm 0.1$   $\chi^2/\text{degrees of freedom} = 0.96$

where  $x = g^2 Y/3$ . Using the fitted values of  $G^4$ ,  $g^2$ , and  $\alpha_B$  yields a total predicted excess for  $\bar{p}p$  over  $pp$  of  $16 \pm 2$  mb in the charged-multiplicity range 4–18. The experimental value is  $7.1 \pm 6.7$  mb,<sup>3</sup> about one standard deviation lower. The model predicts a mean neutral multiplicity half that of the mean charged multiplicity in the same prong range.

The last column in Table II contains the predic-

tion of the model for the mean number of  $\pi^0$ 's produced in annihilation processes as a function of the number of charged pions. The mean number of  $\pi^0$ 's is predicted to be almost independent of the charged-pion multiplicity at these energies. This is in marked contrast to the experimentally observed correlation between the mean number of  $\pi^0$ 's and charged-primary multiplicity in  $pp$  interactions, or in the overall sample of this experi-

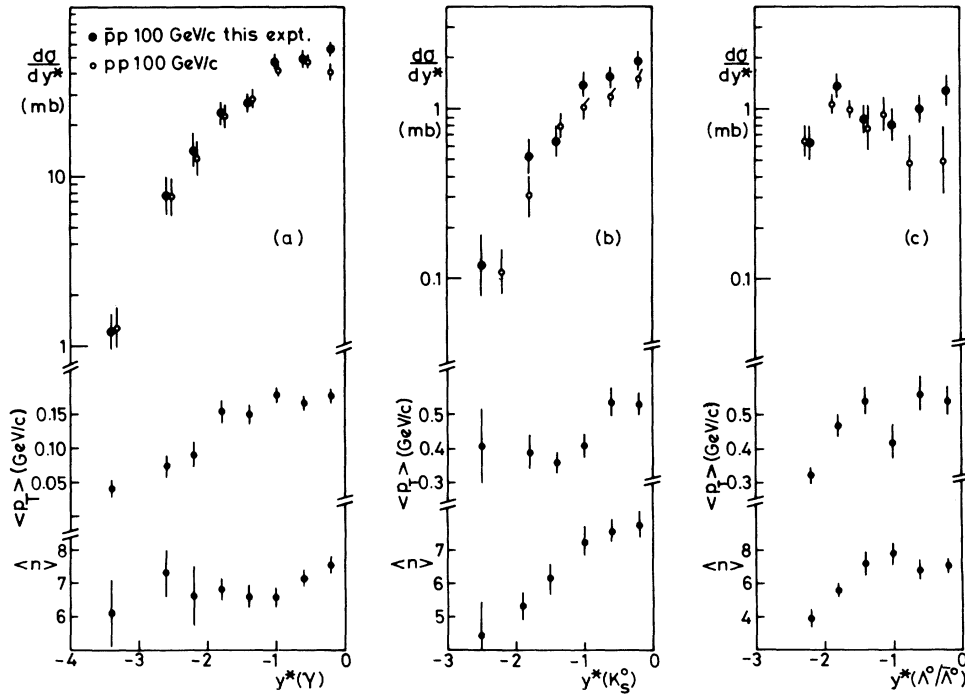


FIG. 3. Center-of-mass rapidity distributions for (a)  $\gamma$ 's, (b)  $K_S^0$ , and (c)  $\Lambda^0$  ( $\bar{\Lambda}^0$ ). The  $pp$  data from Refs. 21 and 22 have been averaged (Ref. 3). Also shown are mean multiplicities and mean transverse momenta as a function of rapidity.

ment.<sup>3</sup> Thus this prediction could prove a useful test of the model, though the errors on ( $\bar{p}p$ - $pp$ ) differences in the present experiment are too large to allow any conclusions to be drawn.

## V. LONGITUDINAL DISTRIBUTIONS

### A. Rapidity distributions

Any attempt to make a detailed comparison of differential distributions between  $\bar{p}p$  and  $pp$  data is difficult, owing to the limited statistics. However, the  $\bar{p}p$  inclusive cross sections are higher than the corresponding  $pp$  values, and the trend of low-energy data tends to reinforce this view. The differential distributions reflect this excess in normalization, but in most cases we cannot attach any dynamical significance to the observed differences in differential distributions,<sup>3</sup> owing to the poor statistics.

Figure 3(a) shows the variation of  $d\sigma/d|y^*|$  vs  $y^*$  for  $\gamma$ 's, where  $y^*$  is the center-of-mass rapidity defined as  $\frac{1}{2}\ln[(E+p_L)/(E-p_L)]$ . The  $pp$  data are also shown.<sup>21,22</sup> The difference of 11 mb occurs mostly in the central region. If this difference persists with higher statistics, then one may conclude that the difference between  $\bar{p}p \rightarrow \pi^0$  and  $pp \rightarrow \pi^0$  is concentrated mostly in the central region.

Figure 3(b) shows the corresponding plot for  $K_S^0$ , again comparing with  $pp$  data.<sup>21,22</sup> Apart from the difference in overall normalization, no significant differences are observed between the  $\bar{p}p$  and  $pp$  data.

Figure 3(c) shows the variation of  $d\sigma/dy^*$  vs  $y^*$  for  $\bar{p}p - \Lambda^0/\bar{\Lambda}^0$  in the backward hemisphere. The  $\bar{\Lambda}^0$  contribution to the  $pp$  data has been estimated by uniformly distributing the  $\bar{\Lambda}^0$  total cross section throughout the range  $-0.5 < y^* < 0.5$ . The  $\bar{p}p - \Lambda^0/\bar{\Lambda}^0$  curve is higher than the  $pp - \Lambda^0/\bar{\Lambda}^0$  curve in the central region. There may thus be an excess of  $\Lambda^0/\bar{\Lambda}^0$  produced in  $\bar{p}p$  interactions in the central region, although any such assertion can only be tentative in view of the current statistical accuracy of this experiment.

Figures 3(a)–3(c) also show the recoiling mean primary charged multiplicity and the mean transverse momentum as a function of the rapidity of the neutral particle. A rise in recoiling multiplicity is observed towards the central region for  $\Lambda^0/\bar{\Lambda}^0$  and  $K_S^0$ . However, one cannot attribute this solely to annihilations, since a similar effect is observed in  $pp$  interactions.<sup>14</sup> The mean transverse momenta show a rise towards  $y^* = 0$  in each case.

### B. Invariant cross sections

Figures 4(a)–4(c) show the invariant distributions

$$F_1(x) = \int \frac{2E d^2\sigma}{\pi\sqrt{s} dx dp_{T^2}} dp_{T^2}$$

for the three types of particles. Also shown are 100-GeV/c  $pp$  data (Ref. 21) and 14.75-GeV/c  $\bar{p}p$  data (Ref. 23). There is evidence for scaling in  $\bar{p}p \rightarrow \Lambda^0$  from 14.75 GeV/c to 100 GeV/c, as can be seen from Fig. 4(c). Scaling has not set in by 14.75 GeV/c for  $K_S^0$ , as can be seen from Fig. 4(b). The 100-GeV/c  $\bar{p}p$  data are quite similar to the 100-GeV/c  $pp$  data; any differences are obscured by errors. This can probably be taken as evidence that  $\bar{p}p$  and  $pp$  data scale according to a common function in the limit of infinite energies.

Also plotted in Fig. 4 are the mean values of  $p_T$  as a function of  $x$ , defined as  $2p_T^*/\sqrt{s}$ . For  $\gamma$ 's and  $\Lambda^0$ 's we observe a drop in  $\langle p_T \rangle$  for small values of  $x$ . For  $K_S^0$ ,  $\langle p_T \rangle$  does not show any significant variation with  $x$ .

To examine scaling in the central region in greater detail, we plot in Figs. 4(d)–4(f)  $F_1(0)$  against  $s^{-1/4}$  for the production of neutrals in  $\bar{p}p$  and  $pp$  interactions.<sup>18,24</sup> According to Mueller-Regge theory  $F_1(0)$  varies as  $a + bs^{-1/4}$  for large  $s$ , where  $a$  and  $b$  are constants. In the case for  $\gamma$  and  $K_S^0$  we see that  $F_1(0)$  in  $\bar{p}p$  is systematically higher than in  $pp$  interactions, and both are still rising with energy up to 100 GeV/c. For  $\Lambda^0$  production, in contrast,  $F_1(0)$  seems to be constant from  $\sim 10$  GeV/c upwards, and about equal in  $\bar{p}p$  and  $pp$  interactions. However, we note that in  $\bar{p}p$  there is equal production of  $\bar{\Lambda}^0$  at  $x=0$ , which is largely absent in  $pp$ , thus indicating an overall excess of hyperon and antihyperon production in the central region in  $\bar{p}p$ . These scaling properties are in contrast with the topological scaling discussed in Sec. IV, where  $\gamma$  and  $K_S^0$  showed good agreement with scaling, while the  $\Lambda^0$  data changed considerably with energy.

### C. Feynman $x$ distributions

Figures 5(a)–5(c) show  $d\sigma/dx$  vs  $x$  for the three types of particles. Also shown are the mean values of the recoiling primary charged multiplicity as a function of  $x$ . A rise in primary multiplicity is once again observed for  $\Lambda^0$ 's toward the central region, whereas little  $x$  dependence is observed for  $\gamma$ 's and  $K_S^0$ 's.

## VI. TRANSVERSE DISTRIBUTIONS

Figure 6(a) plots  $d\sigma/dp_{T^2}$  against  $p_{T^2}$  for  $\gamma$ 's. The data indicate that the difference in normalization between  $\bar{p}p$  and  $pp$  of 11 mb comes preferentially from small values of  $p_{T^2}$  and that the mean value of  $p_{T^2}$  is less for  $\bar{p}p$  than for  $pp$  (see Table III). How-

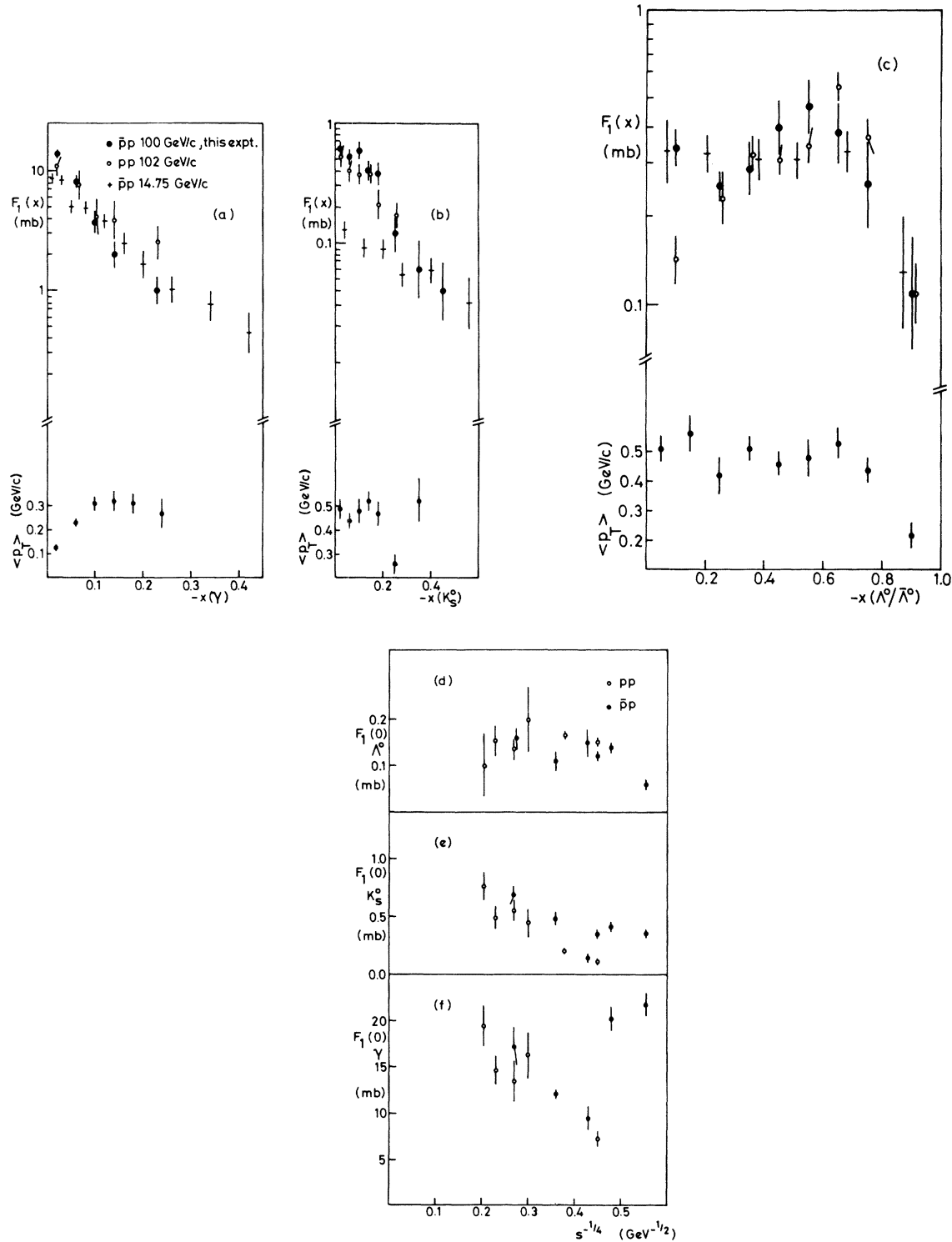


FIG. 4. The invariant cross section

$$F_1(x) = \int \frac{2E d^2\sigma}{\pi\sqrt{s} dx dp_T^2} dp_T^2$$

vs  $x$  for (a)  $\gamma$ , (b)  $K_S^0$ , and (c)  $\Lambda^0$ . Also shown are mean values of  $p_T$  vs  $x$ . (d)  $F_1(0)$  for  $pp \rightarrow \Lambda^0$  and  $\bar{p}p \rightarrow \Lambda^0$  as a function of  $s^{-1/4}$ , (e) for  $K_S^0$ , and (f) for  $\gamma$ .

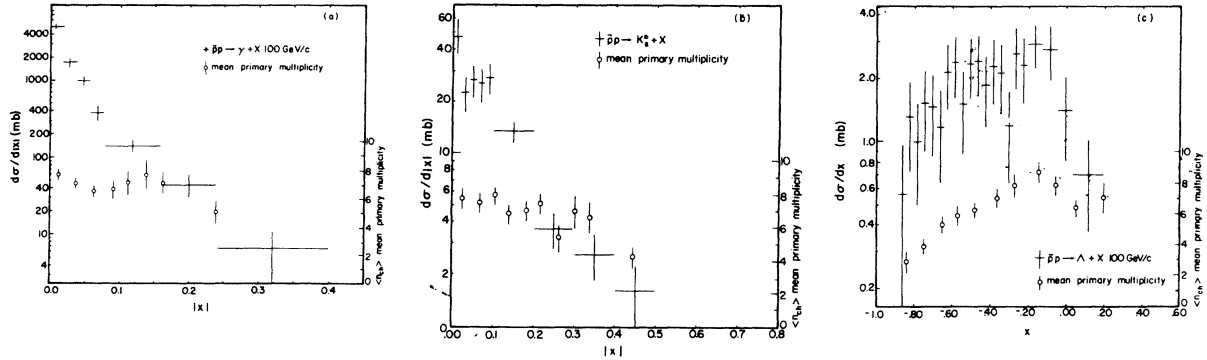


FIG. 5. Feynman  $x$  distribution for (a)  $\gamma$ , (b)  $K_S^0$ , and (c)  $\Lambda^0$ . Also shown are mean values of recoiling primary multiplicity vs  $x$ .

ever, this is in contrast to the well-known result that annihilation processes at lower energy produce secondaries with a larger average transverse momentum than that found in nonannihilation processes.<sup>25</sup>

Figure 6(b) is the corresponding plot for  $K_S^0$ . We see no significant differences in shape between  $\bar{p}p$  and  $pp$ .

Figure 6(c) shows the variation of  $d\sigma/dp_T^2$  vs  $p_T^2$  for  $\Lambda^0$ . Also shown in  $\frac{1}{2}(d\sigma/dp_T^2)$  vs  $p_T^2$  for  $pp$  data.<sup>26</sup> The  $\bar{p}p$  data seem to fall off more sharply than the  $pp$  data. This is reflected in the mean value of  $p_T^2$  for  $\Lambda^0$ , which is  $0.302 \pm 0.023$  for  $\bar{p}p$  compared to  $0.336 \pm 0.035$  for  $pp$ .

The mean values of the recoiling primary multiplicity are plotted as a function of  $p_T^2$  in Figs. 6(a)–6(c). There is a discernible rise in primary multiplicity for higher values of  $p_T^2$  for  $\gamma$ 's and  $K_S^0$  but very little for  $\Lambda^0$ 's. The particle that exhibits the largest change in primary multiplicity in the longitudinal variable exhibits the least change in the transverse variable and vice versa. We also show in Figs. 6(d)–6(f) the variation of  $\langle p_T \rangle$  with multiplicity.  $\langle p_T \rangle$  seems to be independent of multiplicity within errors for  $\gamma$  and  $\Lambda^0$ , while there is some indication of a rise in  $\langle p_T \rangle$  with multiplicity for  $K_S^0$ .

Table III summarizes the mean values of  $p_T$  and  $p_T^2$  for the three types of particle. The mean value of  $p_T$  increases with the mass of the produced particle in a manner similar to  $pp$  data.

#### VII. MOMENTUM-TRANSFER-SQUARED DISTRIBUTION FOR $\Lambda^0$ 'S

Figure 7 shows  $d\sigma/dt'$  vs  $t'$  for  $\Lambda^0$ 's, where  $t' = t - t_{\min}$ , with  $t$  the square of the momentum transfer between the  $\Lambda^0$  and the target proton. A break is observed at a  $|t'|$  value of  $2.8$  (GeV/c)<sup>2</sup>. A maximum-likelihood fit to the functional form

$$\frac{d\sigma}{d|t'|} = A e^{-B|t'|} \quad (10)$$

for the two segments yields the following values of  $A$  and  $B$ :

$$A = 2.26 \pm 0.56 \text{ mb}/(\text{GeV}/c)^2,$$

$$B = 1.28 \pm 0.32 (\text{GeV}/c)^{-2},$$

$$\text{for } |t'| < 2.8 (\text{GeV}/c)^2;$$

$$A = 0.159 \pm 0.033 \text{ mb}/(\text{GeV}/c)^2,$$

$$B = 0.24 \pm 0.05 (\text{GeV}/c)^{-2},$$

$$\text{for } |t'| > 2.8 (\text{GeV}/c)^2.$$

#### VIII. EFFECTIVE MASSES

Figure 8(a) is a plot of  $d\sigma/dM$  vs  $M$ , where  $M$  is the effective mass of the  $K_S^0\pi^*$  combination. Each  $K\pi$  combination is entered once in the plot. All tracks are assumed to be pions at the primary vertex unless the observed ionization favored a proton. We see a pronounced peak near the mass value of the  $K^*(890)$ . To estimate the background, we computed the effective mass by associating each kaon with the charged particles from the next event that has a kaon. The dotted curve in Fig. 8(a) is our estimate for this background. We see that the peak at 890 MeV is almost completely reproduced by the background. We thus see no evidence for  $K^*(890)$  production. No signal was seen in the  $K_S^0\pi^-$  and  $K_S^0\pi^+$  combinations separately. At the one-standard-deviation level we can quote an upper limit  $\sigma(\bar{p}p - K^*(890)) < 0.45$  mb.

Figure 8(b) is the effective-mass distribution for all  $\Lambda^0\pi^*$  combinations, with the background calculated similarly. Some evidence for the production of  $\Sigma(1385)$  is present, and after correcting for branching ratios we estimate a cross section for  $\Sigma(1385)$  production of  $0.24 \pm 0.20$  mb; this oc-



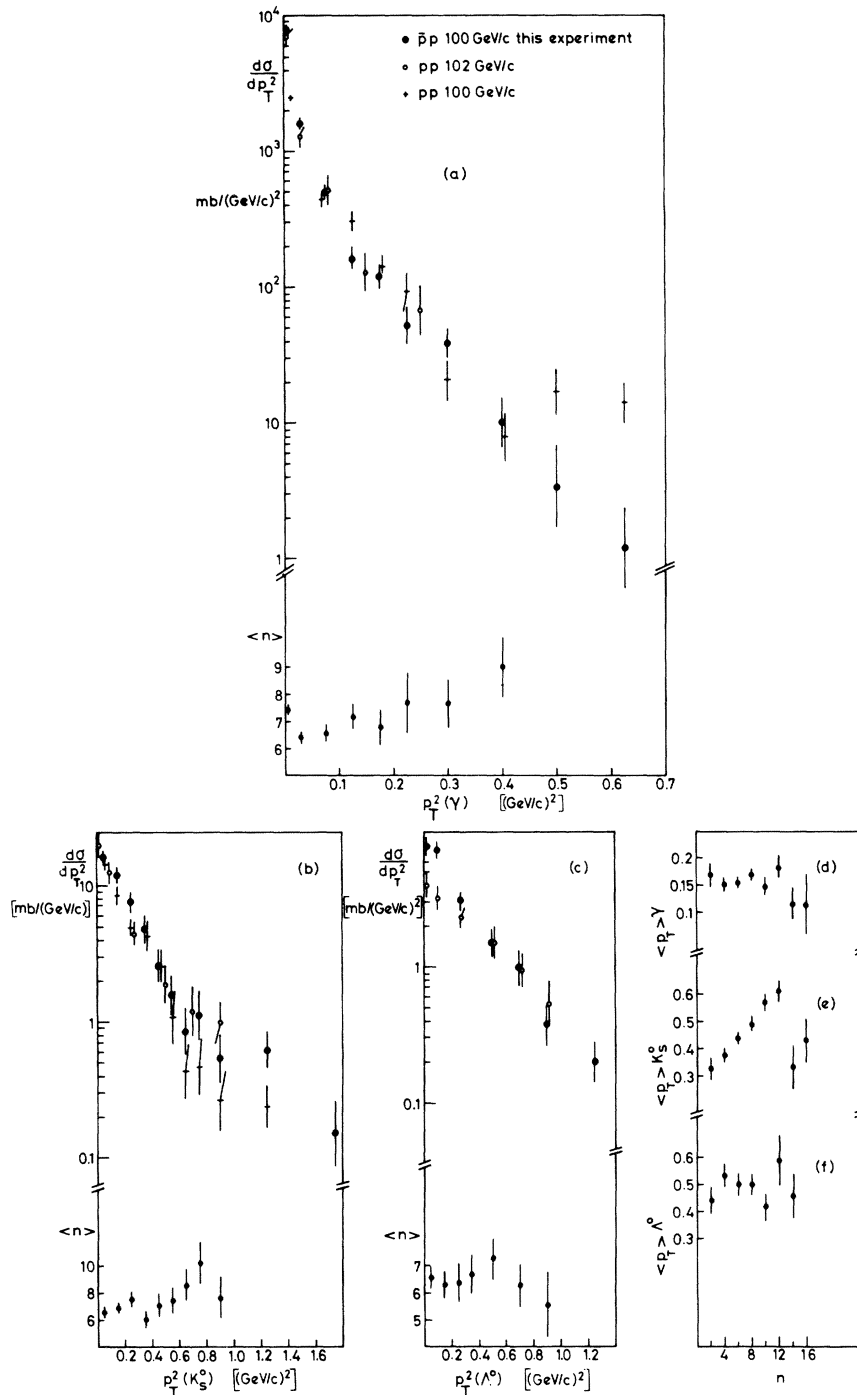


FIG. 6.  $p_T^2$  distribution for (a)  $\gamma$ , (b)  $K_S^0$ , and (c)  $\Lambda^0$ . Also shown are mean values of recoiling primary multiplicity as a function of  $p_T^2$ . (d)  $\langle p_T \rangle$  vs  $n$  for  $\gamma$ 's, (e) for  $K_S^0$ , (f) for  $\Lambda^0$ .

TABLE III. Mean transverse momenta.

	$\bar{p}p$	$\gamma$	$pp^{21,22}$	$\bar{p}p$	$K_S^0$	$pp^{21,22}$	$\bar{p}p$	$\Lambda^0$	$pp^{21,22}$
$\langle p_T \rangle$ (GeV/c)	$0.159 \pm 0.006$	$0.175 \pm 0.020$	$0.175 \pm 0.020$	$0.470 \pm 0.018$	$0.424 \pm 0.043$	$0.424 \pm 0.043$	$0.490 \pm 0.020$	$0.541 \pm 0.060$	$0.541 \pm 0.060$
$\langle p_T^2 \rangle$ $[(\text{GeV}/c)^2]$	$0.043 \pm 0.003$	$0.056 \pm 0.005$	$0.056 \pm 0.005$	$0.295 \pm 0.022$	$0.240 \pm 0.040$	$0.240 \pm 0.040$	$0.302 \pm 0.023$	$0.336 \pm 0.035$	$0.336 \pm 0.035$

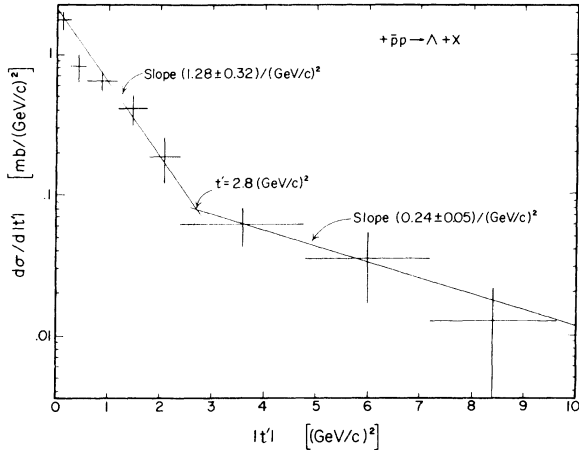
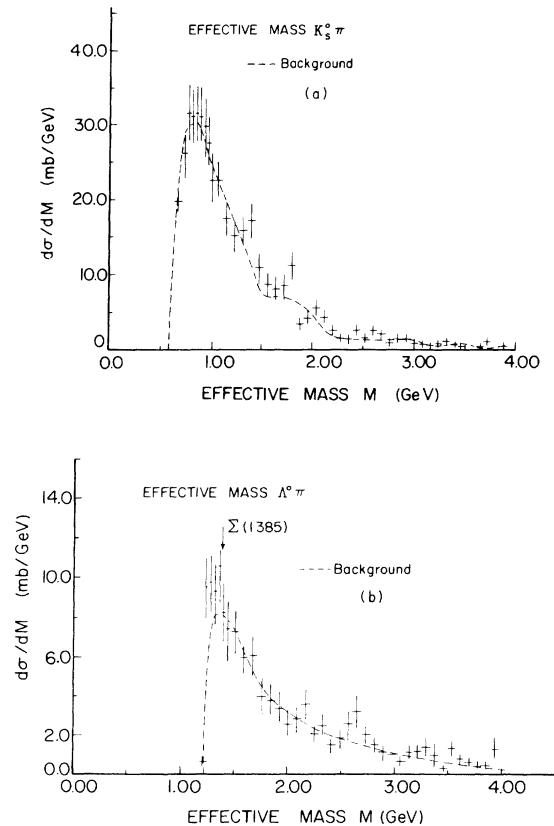
FIG. 7.  $t' = t - t_{\min}$  distribution for  $\Lambda^0$ .

FIG. 8. (a)  $K_S^0 \pi^\pm$  effective-mass distribution. The background has been calculated by associating  $K_S^0$  with the charged particles from the next event with a  $K_S^0$ . (b)  $\Lambda^0 \pi^\pm$  effective-mass distribution. The background has been calculated as in (a).

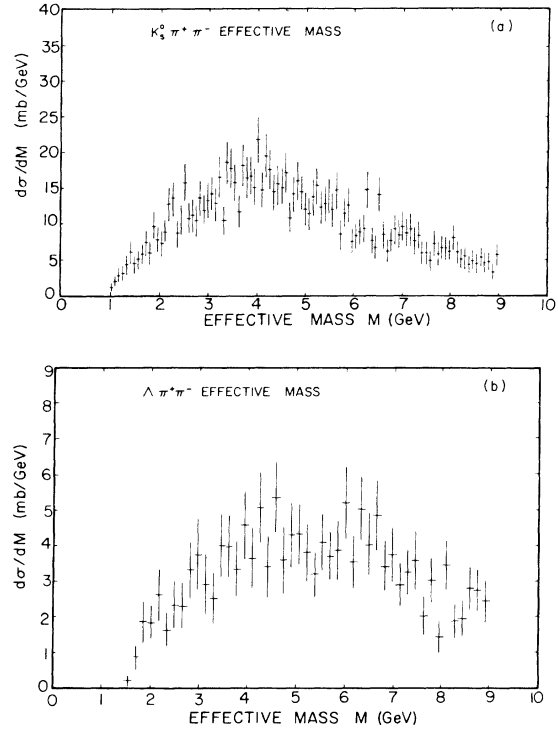


FIG. 9. (a)  $K_S^0 \pi^+ \pi^-$  effective-mass distribution. (b)  $\Lambda^0 \pi^+ \pi^-$  effective-mass distribution.

curs almost entirely in the  $\Lambda^0 \pi^+$  combination.

Figures 9(a) and 9(b) give the effective-mass distribution of  $K_S^0 \pi^+ \pi^-$  and  $\Lambda^0 \pi^+ \pi^-$  combinations, respectively. All charged particles were assumed to be pions unless ionization data favored a proton. No significant peak in either channel is seen.

## IX. MISSING-MASS DISTRIBUTIONS

Figures 10(a)–10(c) give the distribution of the square of the missing mass recoiling from  $\gamma$ 's,  $K_S^0$ 's, and  $\Lambda^0$ 's, respectively. Superimposed is the mean recoiling multiplicity in each case. It can be seen that the mean multiplicity rises with the missing mass squared in much the same way as average multiplicities do with  $s$ . Figure 11 compares the recoiling multiplicities for the three types of missing mass squared with  $\pi^+ p$  and  $K^+ p$  direct-channel data. The data seem to lie on a single universal curve. The agreement is probably better than it seems at first glance, since for the low-lying  $K_S^0$  and  $\Lambda^0$  points the statistics are so poor as to make the estimation of errors in the mean values unreliable. The  $\pi^+ p$  and  $K^+ p$  data have had the elastic two prongs subtracted, whereas for strict comparison they should be included. This should make the agreement between the missing-mass data (which

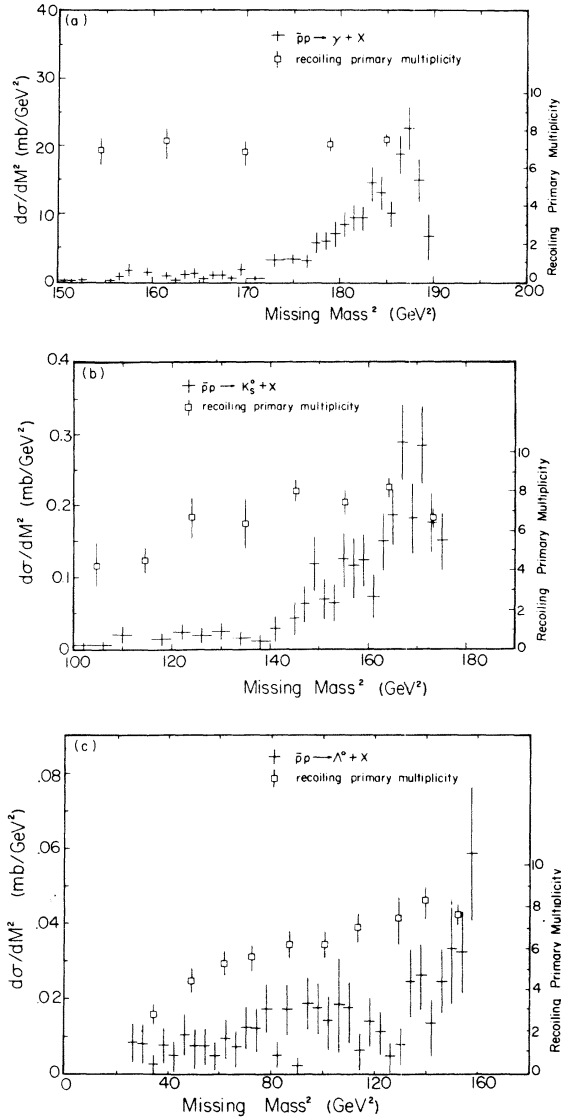


FIG. 10. Missing-mass-squared distribution for (a)  $\gamma$ , (b)  $K_S^0$ , and (c)  $\Lambda^0$ . Also shown is the recoiling charged multiplicity as a function of missing-mass squared.

can be thought of as being due to the scattering of the exchanged particle and the particle at the other vertex) and the direct-channel data even better.

#### X. POLARIZATION

We observe a  $\Lambda^0$  polarization<sup>27</sup> of  $-0.45 \pm 0.21$ . In computing the polarization we have followed the conventions described in Ref. 14. Figure 12 shows the variation of the polarization with Feynman  $x$ . There seems to be a possible trend towards negative values of polarization for  $x$  near  $-1$  and  $0$ . This contrasts with the result obtained for 205-

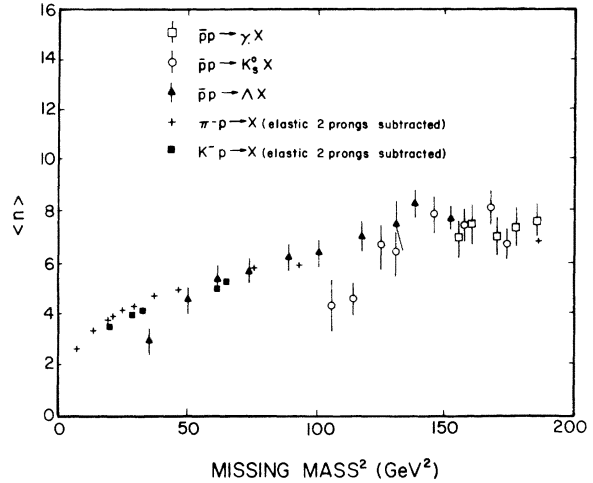


FIG. 11. Comparison of the variation of recoiling multiplicities vs missing-mass squared with direct-channel  $\pi^+p$  and  $K^+p$  data.

GeV/c  $pp$  interactions, where an average  $\Lambda^0$  polarization consistent with zero was observed.<sup>14</sup>

#### XI. MULTIPLE- $V^0$ EVENTS

From events with two or more vees associated we have calculated the cross sections in Table IV for the production of pairs of neutral particles. Here we have used the forward  $K_S^0$  and  $\bar{\Lambda}^0$  and compensated for the losses by artificially increasing their decay weights in the forward hemisphere till the sum of weights in the forward hemisphere was equal to the sum of weights in the backward hemisphere for  $K_S^0$  and  $\Lambda^0$ , respectively.

From the cross section for producing two  $\gamma$ 's we can estimate the correlation function  $f_2^{00}$ ,

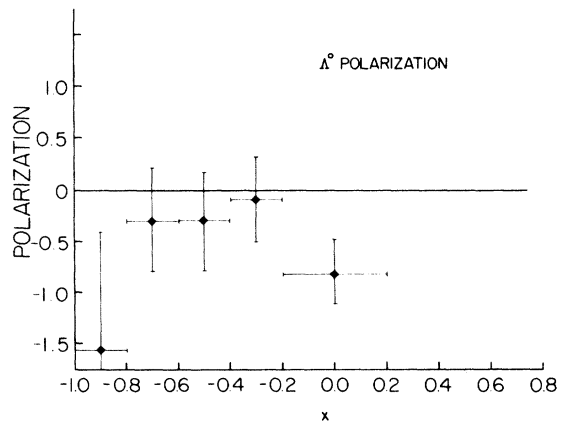


FIG. 12. Polarization of  $\Lambda^0$  vs  $x$ .

TABLE IV. Cross sections for multiple- $V^0$  production.

Channel	No. of events	Cross section (mb)
$\gamma\gamma$	49	$820 \pm 140$
$K_S^0\gamma$	25	$20.8 \pm 4.6$
$\Lambda^0\gamma$	13	$11.2 \pm 3.3$
$\Lambda^0 K_S^0$	8	$0.54 \pm 0.21$
$K_S^0 K_S^0$	11	$0.8 \pm 0.3$
$\Lambda^0 \bar{\Lambda}^0$	4	$0.7 \pm 0.4$

which can be shown to equal

$$f_2^{00} = \frac{\sigma(2\gamma)}{2\sigma_{\text{inel}}} - 0.5\langle n(\pi^0) \rangle - \langle n(\pi^0) \rangle^2 = 3.6 \pm 2.1. \quad (11)$$

We note that  $f_2^{00}$  is larger than  $f_2^{--}$  (Ref. 1) or  $f_2^{0-}$  (Ref. 3). We can also calculate the mean numbers of  $\pi^0$  produced in events with  $\Lambda^0$  or  $K_S^0$  associated:

$$\langle n(\pi^0) \rangle_{K_S^0} = 2.0 \pm 0.5 \quad \langle n(\pi^0) \rangle_{\Lambda^0} = 2.4 \pm 0.7.$$

These values are similar to the overall mean number of  $\pi^0$  produced per inelastic collision:  $2.64 \pm 0.16$  (Ref. 3).

The two-particle inclusive cross sections are given in Table IV.

## XII. CONCLUSIONS

We have examined the production of neutral particles in 100-GeV/c  $\bar{p}p$  interactions. Our main findings are as follows:

(i) The topological cross sections for  $\pi^0$  and  $K_S^0$  production, but not for  $\Lambda^0$ , scale with low-energy data. The multiperipheral model makes a clear prediction for the numbers of  $\pi^0$  produced in annihilations.

(ii) The invariant cross section for  $\Lambda^0$  production scales from 14.75 GeV/c, while  $\gamma$  and  $K_S^0$  do not.

(iii)  $\gamma$  and  $\Lambda^0$  show slightly lower values of  $p_T$  than in  $pp$  interactions at this energy.

(iv) We find evidence of  $\Sigma(1385)$  production, but no significant  $K^*(890)$  signal.

(v) There is evidence of a nonzero  $\Lambda^0$  polarization.

\*Work supported by the United States Energy Research and Development Administration.

†Work supported by the Science Research Council, U.K.

‡Work supported in part by the National Science Foundation, U.S.A.

<sup>1</sup>R. E. Ansorge *et al.*, Phys. Lett. **59B**, 299 (1975).

<sup>2</sup>J. G. Rushbrooke *et al.*, Phys. Lett. **59B**, 303 (1975).

<sup>3</sup>D. R. Ward *et al.*, Phys. Lett. **62B**, 237 (1976).

<sup>4</sup>R. Arnowitt and P. Rotelli, Lett. Nuovo Cimento **4**, 179 (1970).

<sup>5</sup>G. F. Chew, M. Goldberger, and F. Low, Phys. Rev. Lett. **22**, 208 (1968).

<sup>6</sup>P. D. Ting, Phys. Rev. **181**, 1942 (1969).

<sup>7</sup>Y. Eylon and H. Harari, Nucl. Phys. **B80**, 349 (1974).

<sup>8</sup>H. Goldberg, Phys. Rev. D **6**, 2542 (1972).

<sup>9</sup>W. W. Neale, Fermilab Report No. FN-259, 1974 (unpublished).

<sup>10</sup>Reflecting the backward  $\bar{\Lambda}^0$ 's and averaging with the forward  $\Lambda^0$ 's leads to a lower cross section of  $2.04 \pm 0.16$  mb for inclusive  $\Lambda^0$  production.

<sup>11</sup>S. Gjesdal *et al.*, Phys. Lett. **40B**, 152 (1972).

<sup>12</sup>Compilation of  $K^+p$  interactions, CERN-HERA Report No. CERN-HERA 72-2, 1972 (unpublished).

<sup>13</sup>T. M. Knael, DESY Report Nos. 70/2 and 70/3, 1970 (unpublished).

<sup>14</sup>K. Jaeger *et al.*, Phys. Rev. D **11**, 2405 (1975). We note that the authors report a depletion of forward  $\gamma$ 's which is attributed to scanning losses.

<sup>15</sup>Particle Data Group, Phys. Lett. **50B**, 1 (1974).

<sup>16</sup>F. T. Dao and J. Whitmore, Phys. Lett. **46B**, 252 (1973).

<sup>17</sup>D. Cohen, Phys. Lett. **47B**, 457 (1973).

<sup>18</sup>Sources of  $\bar{p}p$  data are the following.

4.6 and 9.1 GeV/c: P. Gregory, paper submitted to international symposium on  $\bar{N}N$  interactions, Stock-

holm, 1976 (unpublished); 12 GeV/c: D. Bertrand *et al.*, work presented at the International Symposium on  $\bar{N}N$  Interactions, Stockholm, 1976 (unpublished); 14.75 GeV/c: Ref. 23; 32 GeV/c: F. Grard, work presented at the International Symposium on  $\bar{N}N$  Interactions, Stockholm, 1976 (unpublished).

<sup>19</sup>C. Bromberg *et al.*, Phys. Rev. Lett. **31**, 1563 (1973).

<sup>20</sup>Only topological data for  $\geq 4$  prongs were used in the fit.

We have assumed that the difference  $\sigma_n(\bar{p}p) - \sigma_n(pp)$  can be attributed to annihilations, and this manifestly is not the case for two prongs, where the difference is negative (Ref. 2). As input to the fit, we have smoothed the values of the differences keeping the normalization constant.

<sup>21</sup>J. W. Chapman *et al.*, Phys. Lett. **47B**, 465 (1973).

<sup>22</sup>M. Alston-Garnjost *et al.*, Phys. Rev. Lett. **35**, 142 (1975).

<sup>23</sup>F. T. Dao *et al.*, Phys. Lett. **51B**, 505 (1974).

<sup>24</sup>Sources of  $pp$  data are the following.

12 and 24 GeV/c: V. Blobel *et al.*, Nucl. Phys. **B69**, 454 (1974); 69 GeV/c: H. Blumenfeld *et al.*, Phys. Lett. **45B**, 525 (1973); *ibid.* **45B**, 528 (1973); 100 GeV/c: Refs. 21 and 22; 205 GeV/c: Ref. 14; 303 GeV/c: A. Sheng *et al.*, Phys. Rev. D **11**, 1733 (1975).

<sup>25</sup>D. Everett *et al.*, Nucl. Phys. **B73**, 440 (1974).

<sup>26</sup>Strictly the comparison should be  $\frac{1}{2} [d\sigma/dp_T^2(\Lambda^0) + d\sigma/dp_T^2(\bar{\Lambda}^0)]$  for  $pp$  but, since the inclusive  $pp \rightarrow \bar{\Lambda}^0$  cross section is only 7% of the  $pp \rightarrow \Lambda^0$  cross section, this should not make too much difference to the comparison.

<sup>27</sup>It must be pointed out that the  $\bar{p}$ 's in this experiment are longitudinally polarized as they are produced by the decay of  $\bar{\Lambda}^0$ 's, though it seems unlikely that this could affect the polarization of  $\Lambda^0$ 's produced backward in the c.m. system.